MAGNETIC RESONANCE IN CHEMISTRY
Magn. Reson. Chem. 2007; **45**: S161–S173
Published online in Wiley InterScience
(www.interscience.wiley.com) DOI: 10.1002/mrc.2162

MRC

Asymmetric doublets in MAS NMR: coherent and incoherent mechanisms

N. R. Skrynnikov*

Department of Chemistry, Purdue University, 560 Oval Drive, West Lafayette, IN 47907-2084, USA

Received 9 July 2007; Revised 22 October 2007; Accepted 2 November 2007

It has been long noted that *J*-resolved doublets observed in solid-state MAS experiments are asymmetric. The asymmetry has been attributed to a *coherent* interference effect involving dipolar and CSA interactions. Recently, Bernd Reif and co-workers suggested that under fast MAS conditions the coherent portion of the effect is suppressed and it becomes possible to observe an *incoherent* mechanism reminiscent of TROSY. The researchers were able to observe the characteristic TROSY-type patterns in $^{15}N–^{1}H^{N}$ spectra of heavily deuterated protein samples (Chevlekov, Diehl, and Reif, previous article in this issue). In the present computer simulation study, we seek to obtain a unified picture of this phenomenon, including both coherent and incoherent aspects. The chosen model focuses on the $^{15}N–^{1}H^{N}$ pair from a polycrystalline sample subject to magic angle spinning. To mimic local dynamics, we assume that the corresponding peptide plane jumps between two orientations. The simulations demonstrate that this simple model reproduces both coherent and incoherent behavior, depending on the MAS speed and the time scale of local dynamics. Furthermore, semianalytical expressions can be derived for both coherent and incoherent (Redfield) limits. Of particular interest is the possibility to use solution-style Redfield results to probe internal protein motions, especially slower motions on the nanosecond time scale. Our simulations show that the differential relaxation measurement permits accurate determination of ^{15}N dipolar-CSA cross correlations already at moderately high MAS speed (*ca* 15 kHz).

KEYWORDS: solid-state MAS spectroscopy; protein dynamics; Redfield theory; dipolar-CSA cross correlations; TROSY; jump model

INTRODUCTION

Asymmetric *J*-resolved doublets were first observed in solid-state magic angle spinning (MAS) spectra of homonuclear $^{13}C–^{13}C$ systems.[1–4] For heteronuclear systems involving protons, such as amide $^{15}N–^{1}H^{N}$, these experiments have been out of reach because of the extensive line broadening. Recently, however, it has been demonstrated that such measurements are possible using deuterated samples with a low content of protons.[5–8] The detailed report of the experimental study is published in this issue of the journal (Chevelkov *et al*. previous article).[9]

Traditionally, the doublet asymmetry in MAS measurements has been viewed as a *coherent* effect, associated with the interplay of dipolar and CSA interactions. This description is fully valid for the sample where there is no internal molecular motion. If, on the other hand, the effects of stochastic local motion are taken into consideration, then it can be expected that an *incoherent* mechanism also contributes to the observed asymmetry. Indeed, such an incoherent mechanism is well known in solution-state spectroscopy where it is responsible for dipolar-CSA cross-correlated cross relaxation.[10–13]

*Correspondence to: N. R. Skrynnikov, Department of Chemistry, Purdue University, 560 Oval Drive, West Lafayette, IN 47907-2084, USA. E-mail: nikolai@purdue.edu

A number of conceptual and practical questions arise in connection to this coherent–incoherent dichotomy. Is it possible to formulate a theoretical treatment embracing both coherent and incoherent effects? Is it possible to separate these two effects on the experimental level? These are the questions that we try to address in the present computer simulation study.

The coherent mechanism responsible for the doublet asymmetry in MAS experiments has been analyzed in some detail.[1–4,14] Consider amide ^{15}N bonded to $^{1}H^{N}$. If the ^{1}H spin is in the state alpha (spin up), then the local magnetic field originating from the $^{15}N–^{1}H^{N}$ dipolar interaction happens to add constructively with the local magnetic field originating from the anisotropy of the chemical shift tensor. The enhanced local field leads to a broad static powder pattern for the $^{15}N–^{1}H^{N}$(alpha) pair. Conversely, in the $^{15}N–^{1}H^{N}$(beta) pair, the CSA and dipolar fields partially cancel each other, leading to a narrow powder pattern. Thus, the Pake doublet consists of the two asymmetric components – one broad and low, the other narrow and tall.[14]

When magic angle spinning is turned on, the spinning sidebands retain the asymmetric pattern. In particular, the two central bands corresponding to the $^{15}N–^{1}H^{N}$(alpha) and $^{15}N–^{1}H^{N}$(beta) pairs are asymmetric. This is the situation where the asymmetric *J*-resolved doublet can be observed

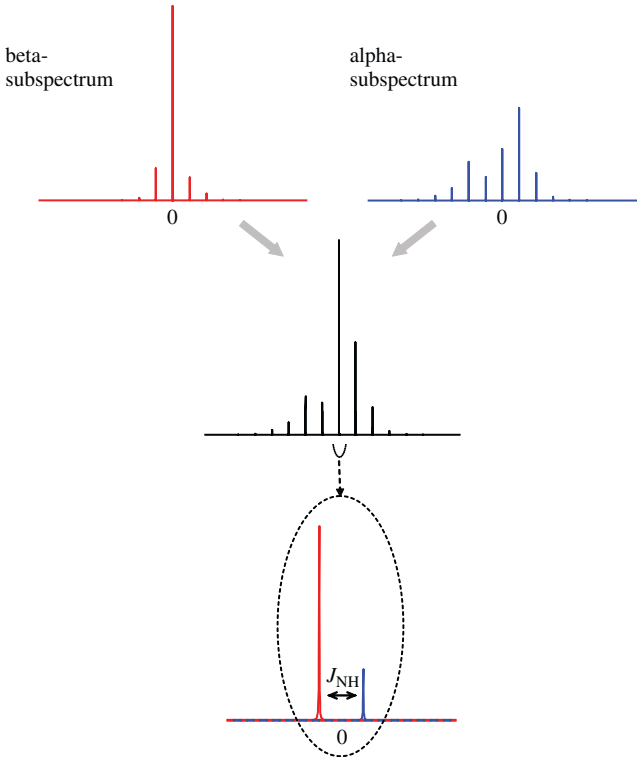

Figure 1. Simulated ^{15}N MAS spectrum ($\omega_R/2\pi = 5$ kHz). Top part – subspectra from ^{15}N–^{1}H^{N}(beta) and ^{15}N–^{1}H^{N}(alpha) spin systems; middle part – full spectrum showing complete spinning sideband pattern; bottom part – expanded view of the central (0-th order) spinning band, featuring the resolved ^{15}N doublet. The simulation was carried out for a system without internal dynamics; other details of the simulation protocol are described in the text. The results have been validated by comparison with the L-COMPUTE algorithm by Helmle and co-workers[15].

in the solid-state MAS spectroscopy, as discussed by Harris and coworkers (see Fig. 1).[1]

On the other hand, the incoherent mechanism responsible for asymmetry in the ^{15}N–^{1}H^{N} doublets has been extensively studied in solution-state spectroscopy on the basis of Redfield relaxation theory.[16,17] In broad terms, the origin of the asymmetry can be described as follows. Transverse ^{15}N magnetization is dephased as a consequence of two consecutive spin transitions triggered by (stochastically modulated) local magnetic field. This local field is comprised of the ^{15}N CSA and dipolar contributions. When the CSA and dipolar components add constructively, such as in the ^{15}N–^{1}H^{N}(alpha) pair, the result is the increase in efficiency of relaxation transitions, which leads, in turn, to a strongly dephased (i.e. broad) signal. Conversely, in the ^{15}N–^{1}H^{N}(beta) pair, the two components of the local field largely cancel out, so that there is little dephasing and the resonance line is narrow and tall. This situation has been exploited to great advantage in the transverse relaxation optimized spectroscopy (TROSY) technique.[13,18]

From the above discussion, it is clear that it is fundamentally one and the same effect – interference of the CSA and dipolar interactions – that is responsible for the doublet asymmetry. In what follows, we discuss a simple model,

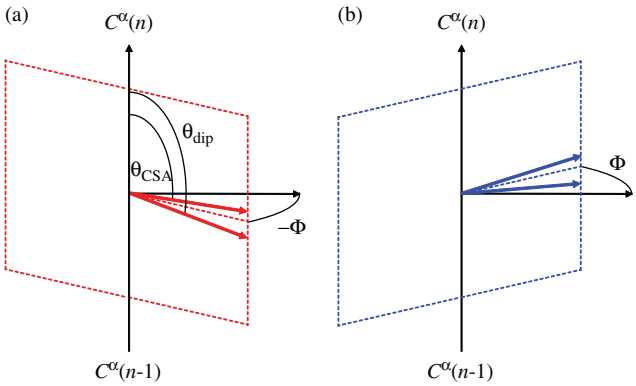

Figure 2. The peptide plane jumps between two orientations in the crystal (C) system of reference. The vector that connects the two 'attachment points' of the peptide plane, $C^{\alpha}(n-1) - C^{\alpha}(n)$, plays the role of the hinge axis. Polar angles $\theta_{dip} = 103^{\circ}$ and $\theta_{CSA} = 83^{\circ}$ define the orientations of the ^{15}N–^{1}H^{N} bond and the unique axis of the ^{15}N CSA tensor respectively (θ_{dip} has been estimated using ultra-high-resolution set of crystallographic coordinates[24]; θ_{CSA} is used as reported in the residual dipolar coupling study[25]). The peptide plane hops between the two orientations, colored in red and blue in the plot and referred to as *a* and *b* in the text, with the amplitude of the jump equal to 2Φ. The populations of the two conformations are assumed to be equal, with forward and backward exchange rates equal to *k*.

which allows to reproduce both coherent and incoherent manifestations of this effect. We further explore a range of experimental situations that can occur in studies of asymmetric doublets by means of fast MAS spectroscopy.

MODEL AND SPECTRAL SIMULATIONS

In view of our proclaimed goal, a model of motion is needed that covers the entire range of dynamic situations: from a rigid molecule to a molecule experiencing fast internal motions that fall into the Redfield limit. One class of models that meets this requirement is based on the stochastic Liouville equation (SLE) method.[19] The SLE formalism had originally been developed for diffusion-type motions and, in particular, for slowly tumbling molecules. However, this approach is computationally expensive and therefore cannot be easily incorporated into MAS simulation, which is itself time consuming. A simple alternative is a jump model, which has been historically introduced to describe chemical exchange.[20] It is well known that exchange models can successfully describe the entire range of dynamics extending from a static limit to the Redfield limit. This has been amply demonstrated in the studies focused on isotropic chemical shifts and also in the studies concerned with other interactions, such as quadrupolar.[21]

For the purpose of this work, we consider a model where a peptide plane executes small-amplitude 'rotational jumps' about the C^{α}—C^{α} axis. This model is close in spirit to the 1D GAF model by Brüschweiler and Wright.[22] Note that fine details of the motional model are usually inconsequential when small-amplitude dynamics is analyzed – often the data

DOI: 10.1002/mrc

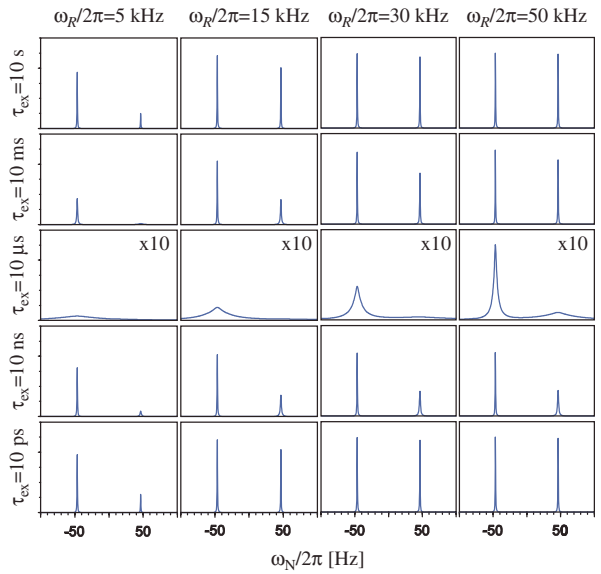

Figure 3. A series of simulated ^{15}N MAS spectra in the presence of small-amplitude local dynamics in a polycrystalline sample. Only the central (0-th order) spinning band, featuring the resolved ^{15}N doublet, is shown in the plot. The amplitude of motion has been kept constant throughout the simulations, $2\Phi = 28^\circ$ (corresponding to the generalized order parameter $S^2 = 0.82$, see below). The equation of motion has been integrated with a step of 1 μs, short enough to assume that the MAS Hamiltonian is time independent. This so-called 'direct' approach to spectral simulations was chosen over other computational tools such as Floquet formalism or various cumulant expansions.[28] Powder averaging was carried out using the sampling scheme by Fliege and Maier.[29] The static magnetic field strength was set to 14.1 T (600 MHz), and the spin system parameters were $J_{HN} = -93$ Hz,[30] $\Delta\sigma_N = -172$ ppm,[31] $r_{HN} = 1.02$ Å. The frequency axis was directed according to the prescription by Levitt[32] (with ppm values increasing toward the left edge of the graph). The intensities and linewidths of the *alpha* and *beta* lines were evaluated using the least-square fitting procedure, where the fitting function consisted of two Lorentzian contours. The quality of the fitting was very good (not shown) except in the case of $\tau_{ex} = 10$ μs.

can be interpreted in a model-free fashion.[23] The geometry of the model adopted in this work is shown in Fig. 2.

For two axially symmetric interactions involving the ^{15}N spin, dipolar ($\lambda = \mathrm{dip}$) and CSA ($\lambda = \mathrm{CSA}$), the Hamiltonians can be represented as follows:

$$H_\lambda(t) = c_\lambda \sum_{m=-2}^{2} (-1)^m F_{-m}(t) T_m^\lambda \qquad (1)$$

where

$$c_{\mathrm{dip}} = -\sqrt{6}\frac{\mu_0}{4\pi}\frac{\gamma_I\gamma_S\hbar}{r_{IS}^3}; \qquad c_{\mathrm{CSA}} = \frac{2}{3}\gamma_S B_0 \Delta\sigma_S$$

and

$$T_0^{\mathrm{dip}} = \frac{1}{\sqrt{6}}(2I_zS_z - \frac{1}{2}(I_+S_- + I_-S_+)); \quad T_0^{\mathrm{CSA}} = S_z$$
$$T_{\pm1}^{\mathrm{dip}} = \mp\frac{1}{2}(I_\pm S_z + I_z S_\pm); \qquad T_{\pm1}^{\mathrm{CSA}} = \mp\sqrt{\frac{3}{8}}S_\pm$$
$$T_{\pm2}^{\mathrm{dip}} = \frac{1}{2}I_\pm S_\pm.$$

Here I and S denote ^{1}H^N and ^{15}N respectively, $\Delta\sigma_S = \sigma_\parallel^S - \sigma_\perp^S$ is the anisotropy of the presumed axially symmetric ^{15}N CSA tensor (defined as shielding), and other notations are standard.[26] In order to specify the spatial part of the Hamiltonians under the conditions of the solid-state MAS experiment, we employ the following four oft-used coordinate frames: principal axes frame (P), where the z-axis coincides with a unique axis of the dipolar or CSA interaction; crystal frame (C), where the z-axis is along the $C^\alpha(n-1)$-$C^\alpha(n)$ vector (see Fig. 2); rotor frame (R), where the z-axis is along the MAS spinning axis; and the laboratory frame, where the z-axis is along the static field B_0.

$$F_m^\lambda(t) = \sum_{q,p=-2}^{2} D_{p,m}^{L\leftarrow R}(0, \beta_{\mathrm{MAS}}, \omega_R t) D_{q,p}^{R\leftarrow C}(\alpha, \beta, \gamma) D_{0,q}^{C\leftarrow P}(\varphi, \theta_\lambda, 0) \qquad (2)$$

Here second-rank Wigner rotation matrices are defined according to Haeberlen,[27] $D_{m',m}(\alpha, \beta, \gamma) = e^{im'\gamma} d_{m',m}(\beta) e^{im\alpha}$ (see Table 2.1 in Ref. 27). The matrix describing coordinate transformation from PAS into the crystal frame, $D_{0,q}^{C\leftarrow P}(\varphi, \theta_\lambda, 0)$, is set up according to the model in Fig. 2. Specifically, θ_{dip} and θ_{CSA} are time-independent, whereas the azimuthal angle φ (the same for both interactions) alternates between $\varphi_a = -\Phi$ and $\varphi_b = \Phi$. Finally, β_{MAS} is the magic angle and ω_R is the sample-spinning angular frequency.

In addition to the dipolar and CSA interactions, J-coupling Hamiltonian is also taken into consideration:

$$H_J = 2\pi J_{IS} I_z S_z \qquad (3)$$

Several approximations are made in the following treatment. First, we neglect the chemical shift difference between the two peptide plane orientations, *a* and *b*, Fig. 2. The main reason for making this approximation is that we wish to focus on the study of dipolar-CSA effects and avoid interference from (trivial) lineshape variations associated with the chemical exchange. Besides, in this study, we are primarily interested in faster (submicrosecond) forms of local dynamics. For motions on this time scale, the modulation of isotropic chemical shift leads only to a small amount of line broadening that can be safely ignored.

Second, we retain only the secular parts of the H_{dip} and H_{CSA} interactions. This approximation is standard for analyses of heteronuclear spin pairs in solid-state experiments. In the context of the present analysis, however, it comes at a price. Specifically, when dipolar and CSA interactions are modulated by very fast stochastic dynamics (Redfield limit), the nonsecular contributions become comparable to secular. Thus, the expressions for Redfield-theory relaxation rates include not only $J(0)$ (a spectral density at zero frequency which originates from the secular portion of the Hamiltonian) but also other terms such as $J(\omega_N)$, which arise from nonsecular components. Those nonsecular contributions are sacrificed in our numeric simulations for the sake of computational speed. Note, however, that the results of our simulations can still be compared with the predictions of the Redfield theory so long as the comparison is limited to the $J(0)$ term. Also, in one of the following sections, which is devoted to the Redfield-type treatment, this restriction is lifted.

DOI: 10.1002/mrc

The evolution of the spin system, including the dynamics (exchange) effects, is treated in the Liouville space endowed with the standard operator basis:

$$\{S_+^a + 2S_+^a I_z^a, S_+^a - 2S_+^a I_z^a, S_+^b + 2S_+^b I_z^b, S_+^b - 2S_+^b I_z^b\} \qquad (4)$$

where the superscripts a and b are used to distinguish two peptide plane orientations. In what follows, the operator modes $S_+ + 2S_+ I_z$ and $S_+ - 2S_+ I_z$ are termed *alpha* and *beta* respectively (this nomenclature refers to the spin states of the proton; the descriptors *alpha*/*beta* are distinctive from α/β, which are reserved for Euler angles). In solution-state spectroscopy, *alpha* and *beta* are frequently referred to as anti-TROSY and TROSY components. Although these terms are convenient, they imply a specific – incoherent – origin of the asymmetry effect and, therefore, are not quite suitable for the purpose of the present discussion.

The Liouville superoperator matrix in the basis of Eqn (4) is

$$\Gamma = -i\begin{bmatrix} \omega_{\mathrm{CSA}}^a + \omega_{\mathrm{dip}}^a + \pi J_{IS} & 0 & 0 & 0 \\ 0 & \omega_{\mathrm{CSA}}^a - \omega_{\mathrm{dip}}^a - \pi J_{IS} & 0 & 0 \\ 0 & 0 & \omega_{\mathrm{CSA}}^b + \omega_{\mathrm{dip}}^b + \pi J_{IS} & 0 \\ 0 & 0 & 0 & \omega_{\mathrm{CSA}}^b - \omega_{\mathrm{dip}}^b - \pi J_{IS} \end{bmatrix} + \begin{bmatrix} -k & 0 & k & 0 \\ 0 & -k & 0 & k \\ k & 0 & -k & 0 \\ 0 & k & 0 & -k \end{bmatrix} - \begin{bmatrix} R_\Sigma^a & R_\Delta^a & 0 & 0 \\ R_\Delta^a & R_\Sigma^a & 0 & 0 \\ 0 & 0 & R_\Sigma^b & R_\Delta^b \\ 0 & 0 & R_\Delta^b & R_\Sigma^b \end{bmatrix} \qquad (5)$$

where $\omega_{\mathrm{CSA}} = c_{\mathrm{CSA}} F_0^{\mathrm{CSA}}(t)$ and $\omega_{\mathrm{dip}} = (c_{\mathrm{dip}}/\sqrt{6}) F_0^{\mathrm{dip}}(t)$ are time-modulated frequencies, which differ between the conformations a and b: in the former case, the expression for $F_0(t)$ contains $\varphi_a = -\Phi$, and in the latter case $\varphi_b = \Phi$, see Eqn (2). k is the exchange rate, which is related to the exchange correlation time as $k = 1/(2\tau_{\mathrm{ex}})$. The last term in Eqn (5) represents additional broadening mechanisms and is comprised of combined in-phase and antiphase rates, $R_\Sigma = (R(S_+) + R(2S_+I_z))/2$, $R_\Delta = (R(S_+) - R(2S_+I_z))/2$. It is assumed that the decay of antiphase coherence is caused in part by spin diffusion involving the amide proton (I). The resulting magnetization leakage is approximated by setting $R(2S_+^a I_z^a) = R(2S_+^b I_z^b) = 4\ \mathrm{s}^{-1}$ according to preliminary experimental data from a sample with a high level of deuteration (Chevelkov and Reif, personal communicaton). At the same time, the in-phase rates are set to zero, $R(S_+^a) = R(S_+^b) = 0$. Indeed, the dephasing of nitrogen magnetization is caused by dipolar and CSA interactions, which are explicitly included in Eqn (5). Hence, there is no need to include an additional leakage term.

The equation of motion with the superoperator matrix Eqn (5) can be numerically integrated in a standard fashion. The series of spectra generated in this manner for variable τ_{ex} and ω_R is shown in Fig. 3. Note that the only meaningful distinction between the *alpha* and *beta* lines in Eqn (5) is the different relative sign of ω_{CSA} and ω_{dip}. Hence, the only fundamental reason for a difference in behavior of the two doublet components is the interplay between the CSA and dipolar interactions, as discussed in the Introduction.

It is convenient to examine the graph in Fig. 3 row by row.

(i) The top row illustrates the case when local dynamics is exceedingly slow, $\tau_{\mathrm{ex}} = 10$ s (this case is equivalent to a situation where dynamics is absent altogether). At low MAS rates, $\omega_R/2\pi = 5$ kHz, one observes a strongly asymmetric doublet. The effect is entirely coherent in origin and is due to the fact that the intensity of the *alpha* and *beta* subspectra is unevenly distributed among the spinning sidebands (*cf* Fig. 1). As MAS rate is increased, the sidebands disappear and the central doublet is rendered symmetric. This is simply a consequence of coherent averaging whereby fast magic angle spinning efficiently scales down both dipolar and CSA interactions. In the next section, we present the semianalytical expressions, which address the case of no internal dynamics.

(ii) The second row illustrates the situation where relatively slow dynamics, $\tau_{\mathrm{ex}}\omega_{\mathrm{dip/CSA}} \gg 1$, leads to the increased doublet asymmetry. It appears that this case has not been investigated experimentally. From a practical standpoint, an experimental study will likely be difficult because at $\tau_{\mathrm{ex}} \sim 10$ ms the lines are usually broadened due to modulation of isotropic chemical shift.

(iii) The third row illustrates the coalescence regime $\tau_{\mathrm{ex}}\omega_{\mathrm{dip/CSA}} \sim 1$. Spectral lines are severely broadened due to modulation of dipolar and CSA interactions by internal motion.

(iv) The fourth row corresponds to the Redfield regime, $\tau_{\mathrm{ex}}\omega_{\mathrm{dip/CSA}} \ll 1$. At lower spinning rates, $\omega_R/2\pi = 5$ kHz, the doublet asymmetry is caused by both coherent and incoherent mechanisms. As MAS rate is increased, the coherent portion is eliminated. At 50-kHz spinning speed, the asymmetry is almost entirely of incoherent origin. In one of the following sections, we demonstrate that the asymmetry can be correctly predicted using the Redfield-theory treatment. With correlation time $\tau_{\mathrm{ex}} = 10$ ns, the cross-correlation effect is sufficiently large to produce the highly asymmetric spectral pattern (rightmost panel in the fourth row).

(v) The fifth row is similar to the fourth row, except the correlation time is much shorter, $\tau_{\mathrm{ex}} = 10$ ps. Under these conditions, the cross-correlation effect is small, and the asymmetry cannot be easily detected (rightmost panel in the fifth row).

The two panels in the upper and lower right corners of Fig. 3 illustrate the effect of coherent and incoherent averaging respectively.[33] In both cases, the observed doublet patterns are sharp and symmetric. Note that coherent

DOI: 10.1002/mrc

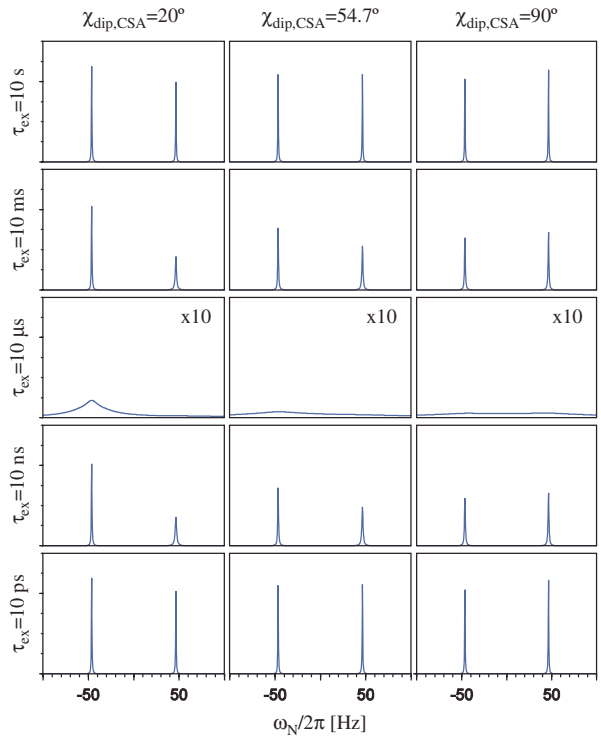

Figure 4. A series of simulated ^{15}N MAS spectra in the presence of small-amplitude local dynamics in a polycrystalline sample. The angle $\chi_{dip,CSA}$ is forcibly changed by varying θ_{CSA} while maintaining θ_{dip} constant, see Fig. 2. The MAS frequency $\omega_R/2\pi$ is 15 kHz; other simulation parameters are the same as in Fig. 3.

averaging is already achieved on the time scale $(\omega_R/2\pi)^{-1} \sim 10\,\mu s$, whereas the incoherent averaging requires a much faster process, $\tau_{ex} \sim 10$ ps. In between these two limiting cases, the efficiency of the MAS averaging is undermined by internal dynamics, as evidenced by the broadened and asymmetric spectral patterns (*cf* right column in Fig. 3). A failure of coherent averaging schemes in the presence of random motion is, of course, a general feature – this is the reason why MAS spectroscopy cannot be used to improve the severely broadened spectra of very large molecules in solution.

One important observation needs to be made with regard to Fig. 3. Let us focus for a moment on the fourth row in the plot, where internal dynamics falls in the Redfield regime and the cross-correlation effects are sufficiently large to allow for experimental detection. The intensity ratio of the *alpha* and *beta* components changes along this row as 0.110, 0.342, 0.385, and 0.395, gradually approaching the value predicted by the Redfield-theory treatment (0.401). Hence, only at higher MAS rates the spectra reflect pure cross-correlation effects akin to TROSY. At lower rates, $\omega_R/2\pi \lesssim 15$ kHz, the data are significantly affected by the *coherent* dipolar-CSA interference. Generally, lineshape analysis is not well suited for studies of cross correlations. In what follows, we discuss an alternative approach that can be successfully employed already with moderately fast MAS, $\omega_R/2\pi \sim 15$ kHz.[9]

In addition to Fig. 3, we also investigated the dependence of spectral patterns on the angle that the dipolar interaction makes with the unique axis of the CSA tensor, $\chi_{dip,CSA}$. In actual peptides, this angle remains nearly constant (to within several degrees).[25,34] Nevertheless, we choose to vary this parameter in order to obtain better insight into the 'addition/subtraction' of the local fields associated with the CSA and dipolar interactions. The results of these simulations are presented in Fig. 4.

For a pair of axially symmetric second-rank tensors, such as the dipolar and CSA interactions, the relative projection is defined as $d_{0,0}(\chi_{dip,CSA}) = P_2(\cos\chi_{dip,CSA})$ (where $P_2(x) = (3x^2 - 1)/2$ is the second-order Legendre polynomial). On a qualitative level, it can therefore be expected that the doublet asymmetry disappears when $\chi_{dip,CSA} = 54.7°$ (magic angle), as the CSA and dipolar interactions are 'orthogonal' in this situation. If the angle is increased further, to $\chi_{dip,CSA} = 90°$, the asymmetry of the doublet should be reversed, i.e. the *alpha* component resonating at 46.5 Hz (at lower ppm value) should become the taller and sharper of the two. These qualitative predictions coincide with the familiar Redfield-theory result, which states that the dipolar-CSA cross correlations are proportional to $P_2(\cos\chi_{dip,CSA})$ for a rigid molecule isotropically tumbling in solution.

In Fig. 4, however, we find certain deviations from the predicted pattern. For instance, a doublet with intensity ratio 0.66 is observed in the case when $\chi_{dip,CSA} = 54.7°$, $\tau_{ex} = 10$ ns (fourth row, middle column in the plot). The value 0.66, which is essentially independent of the MAS speed, differs significantly from the expected ratio, 1.0. The reason for this apparent discrepancy is that the cross-correlation effects in our model originate from strongly anisotropic local motion, see Fig. 2. Mathematically this can be appreciated from the explicit Redfield-theory analysis, which is presented at a later point in the text.

COHERENT LIMIT

In formulating our model, we assumed that the two conformations, *a* and *b*, are degenerate with respect to chemical shift. If so, then in the limit of very slow motion ($k \ll R_\Sigma$) the conformational species *a* and *b* produce identical spectra. In fact, the same spectrum can be generated by considering a single type of conformational species with $\varphi = 0$ ($\Phi = 0$). Hence, in this situation, the exchange can be neglected altogether.

Two simplifications can be subsequently made in the superoperator Eqn (5). First, the exchange part can be dropped according to the discussion above. Second, off-diagonal terms R_Δ in the relaxation matrix can be dropped as well. The latter is possible because these terms are nonsecular and couple two lines resonating at different frequencies. Specifically, this approximation is justified when $R_\Delta \ll 2\pi J_{HN}$ – which is automatically fulfilled as long as the lines in the doublet are sufficiently well resolved. (Note that in this respect transverse cross correlations are different from longitudinal: the latter are strongly affected by the R_Δ term.[35]) Having made these simplifications, we are left with the superoperator, which commutes with itself at different moments in time. Furthermore, the remaining part of the relaxation matrix is trivial

DOI: 10.1002/mrc

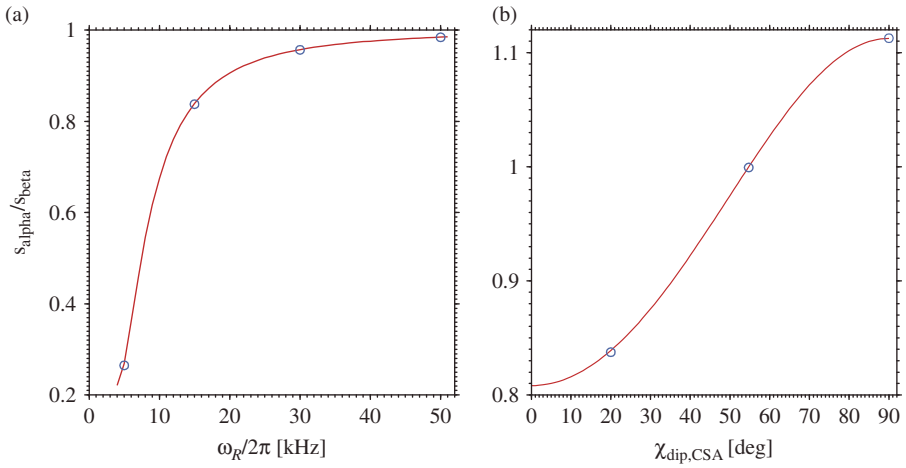

Figure 5. Asymmetry of the ^{15}N doublet, s_{alpha}/s_{beta}, in the limit of coherent evolution (very slow internal dynamics or no dynamics) as a function of (a) MAS speed and (b) the angle between the dipolar and CSA axes. The curves are generated according to Eqns (8–10) for the *beta* component and their equivalents for the *alpha* component. The circles in panels (a) and (b) represent the intensity ratios evaluated directly from the spectra as shown in the top rows of Figs 3 and 4 respectively. To obtain the intensities, the simulated spectra were fitted with a combination of two Lorentzians. Of note, the linewidths of the *beta* and *alpha* components in the coherent limit are equal. This feature has been previously discussed in relation to the entire spinning sideband manifold.[2,4] This is in contrast to the TROSY-type doublets, which display differential line broadening.

(proportional to the unity matrix) and therefore can be ignored. At this point, standard methods can be used to evaluate the relative intensities of the two lines in the doublet.[36,37] Let us focus for a moment on the *beta* line that appears at the frequency $J_{HN}/2 = -46.5$ Hz. The intensity of the NMR spectrum at this frequency is given by

$$s_{beta} = \frac{1}{8\pi^2}\int_0^{2\pi} d\gamma \int_0^{\pi} \sin\beta d\beta \int_0^{2\pi} d\alpha \times \mathrm{Re}\left\{\int_0^{\infty} \mathrm{e}^{-i(\Xi(\alpha+\omega_R t,\beta,\gamma)-\Xi(\alpha,\beta,\gamma))}\mathrm{e}^{-i2\pi(J_{HN}/2)t}dt\right\} \quad (6)$$

where the outer three integrals represent the powder averaging and the inner integral is from the Fourier transformation of the time-domain signal taken at the frequency $J_{HN}/2$. $\Xi(\alpha+\omega_R t,\beta,\gamma)-\Xi(\alpha,\beta,\gamma)$ is the phase acquired by the *beta* coherence precessing at the (time-modulated) angular frequency $\omega_{CSA}-\omega_{dip}-\pi J_{HN}$ (cf. Equation (5)):

$$\Xi(\alpha+\omega_R t,\beta,\gamma)-\Xi(\alpha,\beta,\gamma) = \int_0^t (\omega_{CSA}(\alpha+\omega_R t',\beta,\gamma)-\omega_{dip}(\alpha+\omega_R t',\beta,\gamma)-\pi J_{HN})dt' \quad (7)$$

Upon substitution of Eqn (7) into Eqn (6), the terms containing J_{HN} cancel out. At this point, several standard manipulations can be performed on Eqn (6) making use of the periodicity property for Ξ and replacing the integration variable t with $\tilde{\alpha} = \alpha + \omega_R t$,[37] leading to the final result:

$$s_{beta} = \frac{1}{4\pi}\int_0^{2\pi} d\gamma \int_0^{\pi} \sin\beta d\beta |Q(\beta,\gamma)|^2 \quad (8)$$

$$Q(\beta,\gamma) = \frac{1}{2\pi}\int_0^{2\pi} \mathrm{e}^{-i\Xi(\alpha,\beta,\gamma)}d\alpha \quad (9)$$

$$\Xi(\alpha,\beta,\gamma) = \left\{c_{CSA}\sum_{q,p} d_{p,0}(\beta_{MAS})d_{q,p}(\beta)d_{0,q}(\theta_{CSA})\frac{\sin(p\alpha+q\gamma)}{p\omega_R}\right\} - \left\{(c_{dip}/\sqrt{6})\sum_{q,p} d_{p,0}(\beta_{MAS})d_{q,p}(\beta)d_{0,q}(\theta_{dip})\frac{\sin(p\alpha+q\gamma)}{p\omega_R}\right\} \quad (10)$$

The result for the intensity of the *alpha* component, s_{alpha}, is different only in that the minus sign on the r.h.s. of Eqn (10) should be replaced with the plus (*cf* the precession frequencies: $\omega_{CSA}-\omega_{dip}-\pi J_{HN}$ and $\omega_{CSA}+\omega_{dip}+\pi J_{HN}$ for *beta* and *alpha* coherences respectively). Thus, the ratio s_{alpha}/s_{beta} can be evaluated numerically without resorting to matrix manipulations. The results of such calculations are shown in Fig. 5.

REDFIELD REGIME

We start by deriving the Redfield-theory result for dipolar-CSA cross-correlated cross relaxation in spinning solids. The derivation closely follows the one by Torchia and Szabo[38] except the cross correlations are treated instead of the auto correlations and the model of the local dynamics is slightly altered. In accordance with the general formulation of the Redfield theory, stochastic modulation of spin interactions must be incorporated directly in the Hamiltonians. This can be achieved by replacing the argument φ in $F_m^{\lambda}(t)$, Eqn (2), with $\varphi(t)$. The time dependence in $\varphi(t)$ describes stochastic transitions between the two conformations, $\varphi = \Phi$ and $\varphi = -\Phi$. With this substitution, the cross correlation between the dipolar and

DOI: 10.1002/mrc

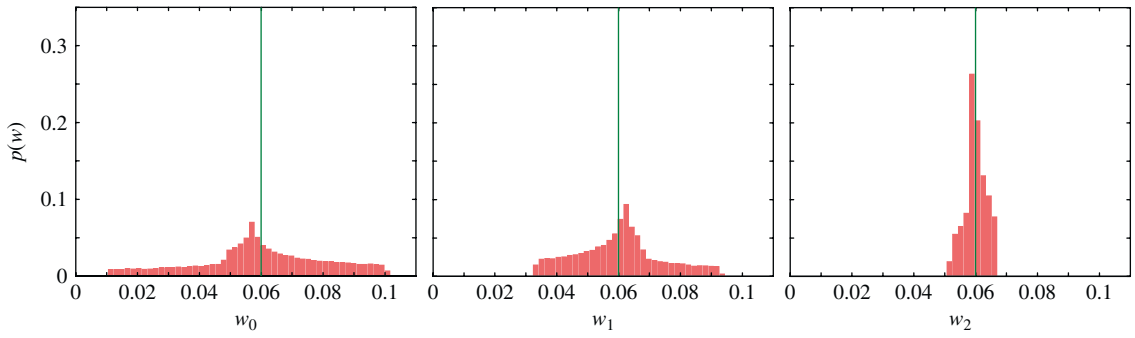

Figure 6. Distribution of the coefficients $w_m(\beta, \gamma)$ in a powder (microcrystalline) sample. Generated using Eqn (16) for the geometry shown in Fig. 2, with $2\Phi = 28^\circ$. Green vertical lines mark the value $\overline{w}$, Eqn (20). In generating these histograms, 100 000 randomly oriented vectors were used to sample, in a uniform fashion, the surface of the unit sphere.

CSA interactions can be spelled out as

$$\begin{aligned} g_m^{\mathrm{dip,CSA}}(\tau) &= < F_m^{\mathrm{dip}}(t) F_m^{\mathrm{CSA}^*}(t+\tau) > \\ &= \sum_{\substack{q,p=-2 \\ q',p'=-2}}^{2} < D_{p,m}^{L\leftarrow R}(0, \beta_{\mathrm{MAS}}, \omega_R t) D_{q,p}^{R\leftarrow C}(\alpha, \beta, \gamma) \\ &\quad \times D_{0,q}^{C\leftarrow P}(\varphi(t), \theta_{\mathrm{dip}}, 0) D_{p',m'}^{L\leftarrow R^*}(0, \beta_{\mathrm{MAS}}, \omega_R(t+\tau)) \\ &\quad \times D_{q',p'}^{R\leftarrow C^*}(\alpha, \beta, \gamma) D_{0,q'}^{C\leftarrow P^*}(\varphi(t+\tau), \theta_{\mathrm{CSA}}, 0) > \end{aligned} \tag{11}$$

The result pertains to a crystallite with orientation (α, β, γ); angular brackets denote averaging with regard to t. Note that in calculating the cross-correlated cross relaxation rates, the two correlation functions appear alongside in the Redfield-theory calculations, $g_m^{\mathrm{dip,CSA}}(\tau)$ and $g_m^{\mathrm{CSA,}dip}(\tau)$. The latter can be obtained from the former by a trivial permutation on the r.h.s. of Eqn (11).

At this point, consider two rate constants that are present in the problem: the rate of exchange, k, and the sample spinning rate, $\omega_R/2\pi$. For the Redfield theory to be valid, k should meet the following condition: $k \gg c_{\mathrm{dip}}/2\pi = 28.1$ kHz. Since in practice the attainable MAS rates do not exceed ca. 50 kHz, this automatically means that $k \gg \omega_R/2\pi$. If so, then the time-average can first be calculated for the fast 2-site exchange process (assuming that a given crystallite is static), and then extended to address a much slower modulation associated with the sample spinning. After a simple rearrangement, the cross-correlation function becomes

$$\begin{aligned} g_m^{\mathrm{dip,CSA}}(\tau) = \sum_{\substack{q,p=-2 \\ q',p'=-2}}^{2} & < D_{p,m}^{L\leftarrow R}(0, \beta_{\mathrm{MAS}}, \omega_R t) \\ & \times D_{p',m'}^{L\leftarrow R^*}(0, \beta_{\mathrm{MAS}}, \omega_R(t+\tau)) \\ & \times D_{q,p}^{R\leftarrow C}(\alpha, \beta, \gamma) D_{q',p'}^{R\leftarrow C^*}(\alpha, \beta, \gamma) \\ & \times d_{0,q}^{C\leftarrow P}(\theta_{\mathrm{dip}}) d_{0,q'}^{C\leftarrow P}(\theta_{\mathrm{CSA}}) \Gamma_{q,q'}(t, t+\tau) > \end{aligned} \tag{12}$$

$$\Gamma_{q,q'}(t, t+\tau) = < e^{iq\varphi(t)} e^{-iq'\varphi(t+\tau)} > \tag{13}$$

The correlation function in Eqn (13) for the 2-site jump model can be readily calculated using the previously reported formalism.[38–40] Assuming that the two conformations are equally populated, one obtains for the model illustrated in Fig. 2:

$$\begin{aligned} \Gamma_{q,q'}(t, t+\tau) = \Gamma_{q,q'}(\tau) &= \cos(q\Phi)\cos(q'\Phi) \\ &\quad + \mathrm{e}^{-2k\tau} \sin(q\Phi)\sin(q'\Phi) \end{aligned} \tag{14}$$

Only the second, time-dependent, portion of the correlation function in Eqn (14) contributes to the Redfield-type relaxation rates.

Having dealt with the time dependence arising from the fast exchange process, we can return to Eqn (11) and address the time dependence associated with sample spinning. Assuming that the MAS rate is much higher than the rate of the dipolar-CSA cross correlation (justified *a posteriori*), it is permissible to perform the averaging over a single MAS period. The integration with respect to $\omega_R t$ leads to the disappearance of the terms with $p \neq p'$ in the sum, Eqn (12). The remaining phase factor $\exp(-ip\omega_R\tau)$ can be approximated as 1 because the correlation function decays over the time interval which is much shorter than the MAS period, $k \gg \omega_R/2\pi$. Finally, combining the correlation functions $g_m^{\mathrm{dip,CSA}}(\tau)$ and $g_m^{\mathrm{CSA,dip}}(\tau)$ and retaining the time-dependent part of $\Gamma_{q,q'}(\tau)$, one obtains

$$G_m(\tau) = w_m(\beta, \gamma)\mathrm{e}^{-2k\tau} \tag{15}$$

$$\begin{aligned} w_m(\beta, \gamma) = \sum_{q,q',p=-2}^{2} & \{d_{p,m}(\beta_{\mathrm{MAS}})\}^2 d_{q,p}(\beta) d_{q',p}(\beta) \mathrm{e}^{i(q-q')\gamma} \\ & \times \{d_{0,q}(\theta_{\mathrm{dip}}) d_{0,q'}(\theta_{\mathrm{CSA}}) + d_{0,q}(\theta_{\mathrm{CSA}}) d_{0,q'}(\theta_{\mathrm{dip}})\} \\ & \times \sin q\Phi \sin q'\Phi \end{aligned} \tag{16}$$

By relabeling the summation indices, it can be easily established that $w_m(\beta, \gamma)$ is real. It is also straightforward to show that $w_{-m}(\beta, \gamma) = w_m(\beta, \gamma)$. Finally, the Redfield-theory result for the dipolar-CSA cross-correlated cross relaxation reads as follows:[12,41]

$$\eta(\beta, \gamma) = \frac{\sqrt{6}}{24} c_{\mathrm{dip}} c_{\mathrm{CSA}} \{4J_0(0) + 3J_1(\omega_N)\} \tag{17}$$

$$J_m(\omega) = w_m(\beta, \gamma) \frac{\tau_{\mathrm{ex}}}{1 + \omega^2 \tau_{\mathrm{ex}}^2} \tag{18}$$

The coefficients $w_m(\beta, \gamma)$ *scale the relaxation rates* depending on the orientation of crystallite relative to the rotor frame. To determine the relaxation response from the sample, one has to sum multiple exponentials originating from the individual crystallites, $\exp(-\eta(\beta, \gamma)t)$.[38,42]

In one important case, however, the treatment can be simplified. If the experiment focuses on the initial portion of the relaxation profile, $\exp(-\eta(\beta, \gamma)t) \approx 1 - \eta(\beta, \gamma)t$, then

DOI: 10.1002/mrc

powder averaging can be applied directly to the relaxation rates (i.e. to the scaling coefficients $w_m(\beta, \gamma)$). Making use of the orthogonality relationship for Wigner matrices and then performing the summation over p,[43] we arrive at the following result:

$$J_m(\omega) = \overline{w}\frac{\tau_{ex}}{1+\omega^2\tau_{ex}^2} \tag{19}$$

$$\overline{w} = \frac{2}{5}\sum_{q=-2}^{2} d_{0,q}(\theta_{dip})d_{0,q}(\theta_{CSA})\sin^2 q\Phi \tag{20}$$

This result closely resembles the expression that can be obtained in solution-state relaxation analyses (except that the part of the correlation function which is modulated by the overall molecular tumbling is absent).[38] It also provides the opportunity to introduce the operational definition of the order parameter:

$$S^2 = \frac{\sum_{q=-2}^{2} d_{0,q}(\theta_{dip})d_{0,q}(\theta_{CSA})\cos^2 q\Phi}{\sum_{q=-2}^{2} d_{0,q}(\theta_{dip})d_{0,q}(\theta_{CSA})} = \frac{\sum_{q=-2}^{2} d_{0,q}(\theta_{dip})d_{0,q}(\theta_{CSA})\cos^2 q\Phi}{P_2(\cos\chi_{dip,CSA})} \tag{21}$$

According to Eqn (21), the jump amplitude $2\Phi = 28°$ used in the simulations throughout this paper corresponds to $S^2 = 0.82$.

It is instructive to test the validity of approximation leading from Eqn (16) to Eqn (20). In Fig. 6, we present the histogram for $w_m(\beta, \gamma)$ generated over the surface of a unit sphere (β, γ). Clearly, the values of w_m form broad distributions: in particular, w_0 varies by a factor of 10. This means that the cross-correlated rates η associated with individual crystallites can be vastly different. In what follows, we examine the effect of $\eta(\beta, \gamma)$ distribution on observable spectra and measurable decay rates.

SPECTRAL SIMULATIONS USING REDFIELD THEORY

The Redfield-theory treatment described in the previous section can be expanded to simulate MAS spectra such as those shown in Fig. 3. In doing so, we suggest that under the conditions of (i) fast internal motion and (ii) fast MAS, the dipolar and CSA interactions make their presence felt only through Redfield-type relaxation terms. Furthermore, we neglect the small relaxation terms that couple *alpha* and *beta* lines precessing at different frequencies (these neglected terms include R_Δ, as well as small dipolar and CSA contributions). Under these assumptions, the free induction decay can be represented as a sum of two components:

$$FID = (f_{alpha}(t) + f_{beta}(t))/2 \tag{22}$$

$$f_{alpha/beta}(t) = \frac{1}{4\pi}\int_0^{2\pi} d\gamma \int_0^{\pi} \sin\beta d\beta \exp\left(\mp i\pi J_{HN}t - \left(R_2^{dip}(\beta,\gamma) + R_2^{CSA}(\beta,\gamma) \pm \eta(\beta,\gamma) + R_\Sigma\right)t\right)$$

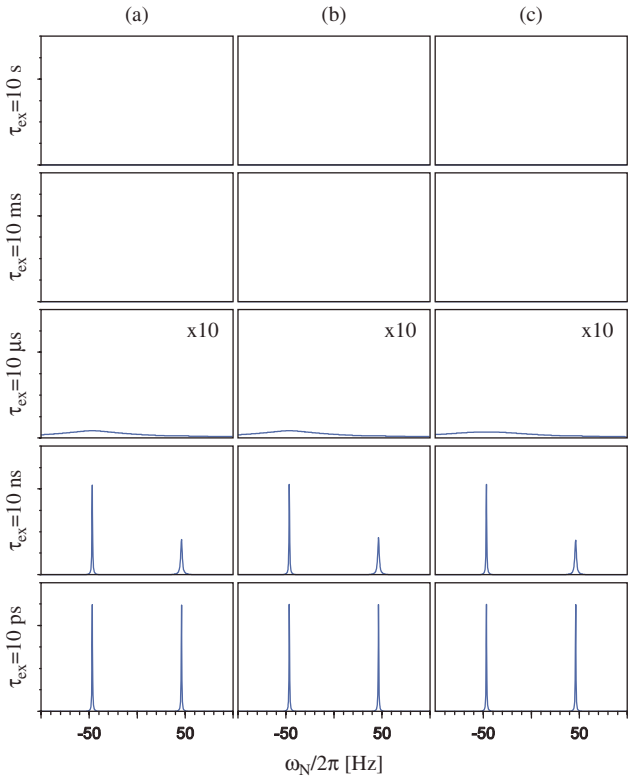

Figure 7. A series of ^{15}N MAS spectra simulated using the Redfield-theory approach. Column (a): the simulations are based on Eqn (22). Column (b): the same as (a), except that only the $J_0(0)$ terms are retained in the relaxation rate constants. Column (c): the same as (a), except that initial slope approximation is used for all relaxation rate constants.

The expressions for orientation-dependent dipolar and CSA transverse relaxation rates, $R_2^{dip}(\beta, \gamma)$ and $R_2^{CSA}(\beta, \gamma)$, can be derived along the same lines as the above result for $\eta(\beta, \gamma)$. For the sake of completeness, the relevant formulas are listed below:

$$R_2^{dip}(\beta,\gamma) = \frac{1}{24}c_{dip}^2\{4J_0(0) + J_0(\omega_H - \omega_N) + 3J_1(\omega_N) + 3J_1(\omega_H) + 6J_2(\omega_H + \omega_N)\} \tag{23}$$

$$R_2^{CSA}(\beta,\gamma) = \frac{1}{4}c_{CSA}^2\{4J_0(0) + 3J_1(\omega_N)\} \tag{24}$$

$$J_m(\omega) = v_m(\beta,\gamma)\frac{\tau_{ex}}{1+\omega^2\tau_{ex}^2} \tag{25}$$

$$v_m(\beta,\gamma) = \sum_{q,q',p=-2}^{2}\{d_{p,m}(\beta_{MAS})\}^2 d_{q,p}(\beta)d_{q',p}(\beta)\cos((q-q')\gamma) \times d_{0,q}(\theta_\lambda)d_{0,q'}(\theta_\lambda)\sin q\Phi\sin q'\Phi \tag{26}$$

$$\bar{v} = \frac{1}{5}\sum_{q=-2}^{2} d_{0,q}(\theta_\lambda)d_{0,q}(\theta_\lambda)\sin^2 q\Phi \tag{27}$$

The coefficients $v_m(\beta, \gamma)$ are calculated with $\theta_\lambda = \theta_{dip}$ or $\theta_\lambda = \theta_{CSA}$, depending on the rate constant in question. In the case when the initial slope approximation is applied, $v_m(\beta, \gamma)$ is replaced with $\bar{v}$.

The calculated FID, Eqn (22), can be readily Fourier transformed, leading to the asymmetric doublet pattern where

DOI: 10.1002/mrc

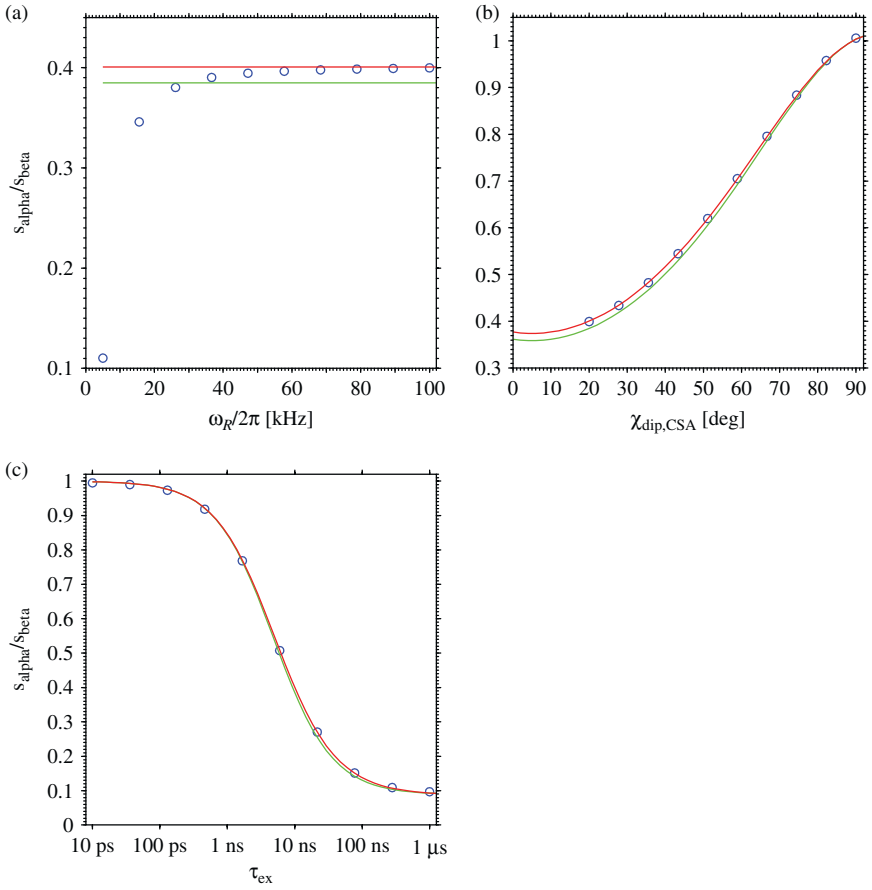

Figure 8. Asymmetry of the ^{15}N doublet, s_{alpha}/s_{beta}, as a function of (a) MAS speed, (b) the angle between the dipolar and CSA axes, and (c) exchange correlation time. Red curves represent the results of the Redfield-theory treatment (derived from the spectra such as shown in Fig. 7, column (b)). Green curves represent the simplified solution based on the initial slope approximation (*cf* spectra in Fig. 7, column (c)). Blue circles represent the outcome of numeric simulations (cf. spectra in Figs 3 and 4). The parameters used in the simulations are as follows: (a) $\tau_{ex} = 10$ ns, $\chi_{dip,CSA} = 20^{\circ}$; (b) $\omega_R/2\pi = 100$ kHz, $\tau_{ex} = 10$ ns; (c) $\omega_R/2\pi = 100$ kHz, $\chi_{dip,CSA} = 20^{\circ}$. Other parameters are the same as described in the caption of Fig. 3.

each line is comprised of multiple Lorentzians. The results are shown in Fig. 7. In principle, the spectra generated in this fashion can be compared with the results of extended numeric simulations, Fig. 3. Specifically, the leftmost column from Fig. 7 can be compared with the rightmost column in Fig. 3, which corresponds to the ultrafast MAS conditions. Such a comparison shows that for $\tau_{ex} = 10$ ps and 10 ns, the spectra appear very similar, whereas for $\tau_{ex} \geq 10$ µs the Redfield approach breaks down and cannot correctly reproduce the spectra. The failure of the Redfield formalism in the slow motion regime is the intrinsic feature of the theory.[44]

As a next step, we would like to move beyond the visual inspection and perform a quantitative comparison of the spectra. At this point, however, it should be recalled that in our numeric simulations, Figs 3 and 4, we used the truncated version of the dipolar and CSA Hamiltonians. Therefore, in order to obtain a clean comparison, the Redfield-theory results should be adjusted accordingly. Specifically, only the $J_0(0)$ terms should be retained in the expressions for $\eta(\beta, \gamma)$, $R_2^{dip}(\beta, \gamma)$, and $R_2^{CSA}(\beta, \gamma)$.

Pursuing this agenda, we regenerated the spectra using the truncated versions of the relaxation rates (Fig. 7, column (b)). This step deserves some additional comments. First, it is needed only for the purpose of comparison, as we seek to confirm the agreement between the Redfield-theory treatment and the numeric simulation using matrix propagators. Second, the predicted doublet patterns remain essentially unchanged when spectral densities other than $J_0(0)$ are discarded (*cf* columns (a) and (b) in Fig. 7). This is indeed not surprising – when τ_{ex} is equal to 10 ns, the relaxation rates η, R_2^{dip}, and R_2^{CSA} are all dominated by $J_0(0)$ (on the other hand, when $\tau_{ex} = 10$ ps, these rates are negligibly small). Thus, the approximation involving $J_0(0)$ plays mainly a technical role and has no major significance in the context of the present analyses.

We used the spectra such as those shown in Fig. 7, column (b), and in Fig. 3 to perform a quantitative comparison. As before, we focused on the line intensity ratio, s_{alpha}/s_{beta}, to characterize the spectra. The results are presented in Fig. 8. First of all, the data demonstrate that there is indeed an excellent agreement between the outcome of the numeric simulations and the Redfield-theory treatment. This agreement, however, is only achieved under ultrafast MAS conditions, $\omega_R/2\pi = 100$ kHz. In contrast, at moderately high MAS rates, there are significant deviations between the numeric results and the Redfield-theory predictions (see

DOI: 10.1002/mrc

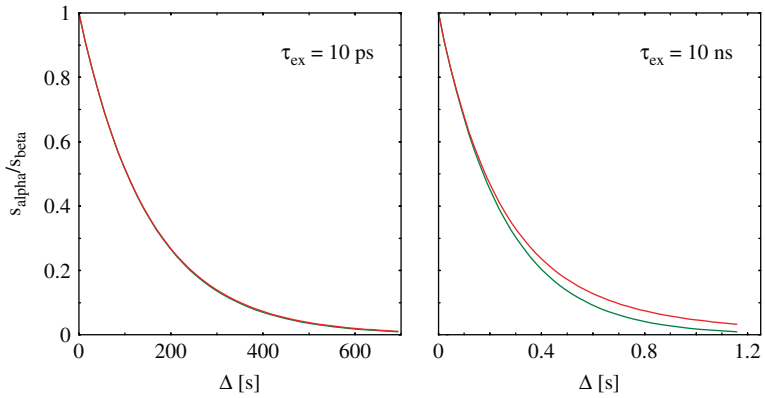

Figure 9. The doublet asymmetry, s_{alpha}/s_{beta}, as a function of time Δ. The data are simulated according to Eqn (28) or, alternatively, approximate Eqn (29) (red and green curves, respectively) for $\tau_{ex} = 10$ ps and 10 ns. The two outcomes illustrated in this figure are characteristic of the systems in the extreme narrowing limit, $\omega_N \tau_{ex} \ll 1$, and in the macromolecular limit, $\omega_N \tau_{ex} \gg 1$. These outcomes are, in a good approximation, insensitive to variation of other model parameters, such as Φ.

panel (a) in Fig. 8). For example, at $\omega_R/2\pi = 15$ kHz, the actual asymmetry of the doublet is 15% lower than the value predicted by the Redfield theory.

$$s_{alpha}/s_{beta} = \int_0^{2\pi} d\gamma \int_0^{\pi} \sin\beta d\beta \exp\left(-\left(R_2^{dip}(\beta,\gamma) + R_2^{CSA}(\beta,\gamma) + \eta(\beta,\gamma)\right)t\right) \Big/ \int_0^{2\pi} d\gamma \int_0^{\pi} \sin\beta d\beta \exp\left(-\left(R_2^{dip}(\beta,\gamma) + R_2^{CSA}(\beta,\gamma) - \eta(\beta,\gamma)\right)t\right) \quad (28)$$

In the context of dynamics studies, it is clearly desirable to stay within the framework of the Redfield formalism. From this perspective, the lineshape analysis is not the most attractive option. In the next section, we discuss the measurement scheme that is better suited for measurement of cross-correlation effects in solids.[9]

DIFFERENTIAL RELAXATION MEASUREMENTS

There are a number of different ways to probe the dipolar-CSA cross-correlation effects. The simplest method relies on difference in line widths between the two components of asymmetric doublet. In practice, however, it is difficult to quantify small line width variations. Alternatively, many experiments target the transfer of magnetization from the in-phase S_+ coherence to the antiphase $2S_+I_z$.[12,41] In the context of this study, we focus on the experimental scheme that monitors the differential relaxation of the two doublet components, $S_+ + 2S_+I_z$ and $S_+ - 2S_+I_z$ (*alpha* and *beta* lines). This scheme has been used for measuring dipolar-CSA cross correlations in the experimental study by Chevelkov *et al.*[9] (previous article in this issue of the journal).

Consider the pulse sequence where *alpha* and *beta* components evolve through the spin-echo period, $\Delta/2 - 180^\circ(S) - \Delta/2$, followed by the indirect-dimension evolution period.[45] The 180° pulse in the middle of the spin-echo element suppresses the ^{15}N chemical shift and ^{15}N–^{1}H^N scalar coupling evolution, while preserving the cross-correlated cross relaxation η. Using this sequence, a series of spectra are recorded for different settings of Δ and the ratios s_{alpha}/s_{beta} are extracted from these spectra. The resulting decay profile, s_{alpha}/s_{beta} *versus* Δ, can be modeled based on Eqn (22):

Furthermore, if the initial-slope approximation is applied, Eqn (28) is reduced to

$$s_{alpha}/s_{beta} = \exp(-2\overline{\eta}\Delta) \quad (29)$$

where $\overline{\eta}$ is calculated according to Eqns (17, 19) and the decay profile, s_{alpha}/s_{beta} *versus* Δ, is assumed to be normalized such that it originates at 1.0.

The quality of the approximation in Eqn (29) relative to the more rigorous result in Eqn (28) is illustrated in Fig. 9. As it turns out, in the case of fast internal dynamics, $\tau_{ex} = 10$ ps, the results are nearly identical. On the other hand, for slower motions, $\tau_{ex} = 10$ ns, there is an appreciable difference. Specifically, the effective decay rates, as obtained from single-exponential fitting of the data in the right half of Fig. 9, differ by 11%. Of course, any such estimate depends on the sampling of the decay profile. In practice, only the initial portion of the curve can be monitored – the observations at longer Δ are not feasible because both components of the doublet are subject to relatively fast relaxation $R_2^{dip} + R_2^{CSA} + R_\Sigma$. Fortunately, the initial portion of the decay curve is very well reproduced by the initial slope approximation (cf. red and green profiles in the right half of Fig. 9). Thus, the initial slope approximation discussed by Torchia and Szabo[38] is directly relevant for the current measurement scheme.

The two panels in Fig. 9 represent two characteristic cases that are likely to be encountered in studies of backbone dynamics in solids. The data in the left panel are generated using the following motional parameters: $\Phi = 14^\circ (S^2 = 0.82)$, $\tau_{ex} = 10$ ps. These values are typical

DOI: 10.1002/mrc

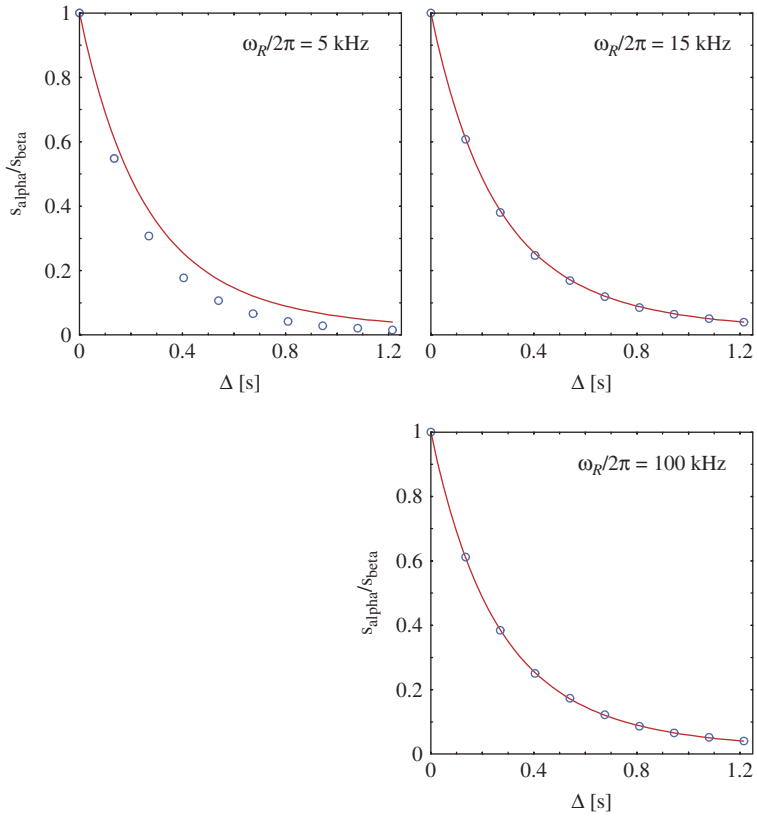

Figure 10. The doublet asymmetry $s_{\text{alpha}}/s_{\text{beta}}$ as a function of time Δ simulated for the $\Delta/2 - 180^\circ - \Delta/2 - t_1$ measurement scheme, $\tau_{\text{ex}} = 10$ ns. The data represented by circles are from the numeric simulation. The data represented by curves are generated according to Eqn (28), where only the terms proportional to $J_0(0)$ are retained in the expressions for relaxation rate constants.

for *solution-state* ^{15}N relaxation studies of globular proteins and are characteristic of small-amplitude fast motions of a peptide plane. It can be fully expected that such fast local dynamics are also present in the *solid-state* samples, assuming that (i) the solid sample is well hydrated and (ii) solid-state measurements are conducted near room temperature. As it turns out, the cross-correlation effect in this situation is far too small to be observed experimentally ($\overline{\eta} = 0.003\ \text{s}^{-1}$ for the data in the left half of Fig. 9). It can therefore be suggested that, for most of the residues, and especially for highly constrained residues from secondary-structure elements, the effect is beyond the detection limit of the modern MAS experiments.

The right panel in Fig. 9 represents a different type of dynamic behavior. In this case, the correlation time of the local motion is 1000-times longer, $\tau_{\text{ex}} = 10$ ns. Nanosecond motions in proteins have been detected both by solution-[46,47] and solid-state methods.[42,48–50] These motions are usually associated with loops and termini. (They can also occur in the structured regions, but the corresponding amplitudes appear to be small in this case.[51]) For the data shown in the right panel of Fig. 9, the calculated cross-correlation rate constant is $\overline{\eta} = 2.0\ \text{s}^{-1}$. The effect of this magnitude lends itself to experimental observation. Thus, we conclude that the MAS experiment employing the $\Delta/2 - 180^\circ - \Delta/2$ element should allow for experimental detection of dipolar-CSA cross correlations in solids. The effect is likely to be limited to a small number of residues featuring a significant amount of nanosecond time-scale dynamics. These residues are most likely to be found in the loops and terminal regions.

It is useful to verify the results of Fig. 9 by comparing them with the outcome of the full-fledged numeric simulation. For this purpose, the program used for lineshape simulations has been expanded. The new program traces the propagation of the spin density matrix during the spin-echo period $\Delta/2 - 180^\circ - \Delta/2$ and the subsequent evolution period t_1. The resulting time-domain response is Fourier-transformed to produce a spectrum similar to that shown in Fig. 3. The simulated doublet is consequently fitted with a pair of Lorentzians and the ratio $s_{\text{alpha}}/s_{\text{beta}}$ is obtained. The simulations are then repeated for different lengths of the relaxation period Δ, yielding the differential relaxation curve (blue circles in Fig. 10).

The inspection of Fig. 10 reveals that, at low spinning speed, $\omega_R/2\pi = 5$ kHz, a sizeable discrepancy still exists between the predictions of the Redfield theory and the results of the numeric simulations. However, already for $\omega_R/2\pi = 15$ kHz the agreement becomes excellent. The significance of this result is that already at moderately high spinning speed, the $\Delta/2 - 180^\circ - \Delta/2 - t_1$ measurement scheme delivers the data that are fully consistent with the Redfield-theory predictions. This is in favorable contrast to the lineshape analyses discussed in the previous section. From the experimental standpoint, this means that the cross-correlation effects can be conveniently studied without the need for ultra-fast MAS.

DOI: 10.1002/mrc

Figure 10 illustrates the experimentally relevant situation, where $\tau_{ex} = 10$ ns. The same trends, however, are observed in the case of fast local dynamics, $\tau_{ex} = 10$ ps (not shown). Of note, the decay profiles similar to those shown in Fig. 10 can be also obtained for systems with much slower dynamics, which fall on the 'slow' side of the coalescence point (*cf* spectra in the second row of Fig. 3). This latter case, though, is of limited practical interest – the spectra of the systems undergoing exchange on the scale of 10 ms are usually badly broadened due to chemical shift modulation. It is worth mentioning, however, that the problem of distinguishing between the 'fast' and 'slow' exchange regimes is a familiar one.[52,53] In the context of the present study, temperature dependence could, in principle, be used to resolve the ambiguity.

CONCLUSIONS

Throughout its history, solid-state NMR has been an extremely valuable source of information on molecular dynamics.[21,54] The development of fast MAS probes opened the way to high-resolution spectroscopy of biological macromolecules, including proteins. Progress in the development of pulse sequences and isotopic labeling schemes made it possible to target the entire gamut of protein spin systems. Today, solid-state MAS measurements can be used to probe protein dynamics on a per-residue basis much in the same fashion as solution-state spectroscopy.[42,55]

Particularly attractive is the possibility to interpret the data from solid-state MAS relaxation measurements within the framework of the Redfield formalism. The apparatus of the Redfield theory and a variety of adjunct motional models were developed primarily for use in solution-state studies. When these results are adapted for solid-state applications, it is important to be aware of their potential limitations.

In this communication, we focus on one particular application concerned with asymmetric $^{15}N-^{1}H^{N}$ doublets. In solutions, the observations of asymmetric $^{15}N-^{1}H^{N}$ doublets let to invention of the popular TROSY technique.[13] The original TROSY experiment can be fully understood on the basis of the Redfield theory. In solids, however, the situation is more complex: the asymmetry may arise through *coherent* as well as *incoherent* (Redfield) mechanisms. Here we demonstrated that both mechanisms can be reproduced within one simple computational model. On the basis of this model, useful semianalytical expressions can be obtained for both the coherent limit and the Redfield limit.

Focusing on the Redfield limit, we found that $\Delta/2 - 180^{\circ} - \Delta/2 - t_1$ measurement scheme, as used by Reif and coworkers,[9] is well suited for measuring the dipolar-CSA cross-correlation effects. While the decay profiles recorded in this MAS experiment are, strictly speaking, multiexponential, they can be also analyzed with reasonable accuracy (several percentage points) using the monoexponential approximation.[38,42] Such a simplified treatment is closely related to the solution-state relaxation analyses. In practice, it is expected that the dipolar-CSA cross-correlation effects can be reliably measured for those amide sites that are involved in nanosecond time-scale local motions. This is particularly promising since studies of nanosecond dynamics by solution-state methods are often faced with significant challenges.[47,56,57]

Acknowledgements

I thank Bernd Reif for suggesting this problem to me, explaining many important concepts, and sharing the experimental data prior to publication. I am also grateful to Veniamin Chevelkov for helpful discussions and to Yi Xue for assembling and setting up the dual-core Xeon processor workstations used for the computations. This study was supported in part by the NSF CAREER grant 044563.

REFERENCES

1. Harris RK, Packer KJ, Thayer AM. *J. Magn. Reson.* 1985; **62**: 284.
2. Nakai T, McDowell CA. *Mol. Phys.* 1992; **77**: 569.
3. Nakai T, McDowell CA. *J. Chem. Phys.* 1992; **96**: 3452.
4. Duma L, Hediger S, Lesage A, Sakellariou D, Emsley L. *J. Magn. Reson.* 2003; **162**: 90.
5. Reif B, Jaroniec CP, Rienstra CM, Hohwy M, Griffin RG. *J. Magn. Reson.* 2001; **151**: 320.
6. Morcombe CR, Gaponenko V, Byrd RA, Zilm KW. *J. Am. Chem. Soc.* 2005; **127**: 397.
7. Chevelkov V, Rehbein K, Diehl A, Reif B. *Angew. Chem. Int. Ed.* 2006; **45**: 3878.
8. Chevelkov V, Faelber K, Schrey A, Rehbein K, Diehl A, Reif B. *J. Am. Chem. Soc.* 2007; **129**: 10195.
9. Chevelkov V, Diehl A, Reif B. *Magn. Reson. Chem.* 2007; this issue.
10. Shimizu H. *J. Chem. Phys.* 1964; **40**: 3357.
11. Mackor EL, MacLean C. *J. Chem. Phys.* 1966; **44**: 64.
12. Tjandra N, Szabo A, Bax A. *J. Am. Chem. Soc.* 1996; **118**: 6986.
13. Pervushin K, Riek R, Wider G, Wüthrich K. *Proc. Natl. Acad. Sci. U.S.A.* 1997; **94**: 12366.
14. Zilm KW, Grant DM. *J. Am. Chem. Soc.* 1981; **103**: 2913.
15. Helmle M, Lee YK, Verdegem PJE, Feng X, Karlsson T, Lugtenburg J, de Groot HJM, Levitt MH. *J. Magn. Reson.* 1999; **140**: 379.
16. Blicharski JS. *Phys. Lett. A* 1967; **24**: 608.
17. Goldman M. *J. Magn. Reson.* 1984; **60**: 437.
18. Yang DW, Kay LE. *J. Biomol. NMR* 1999; **13**: 3.
19. Freed JH. *J. Chem. Phys.* 1968; **49**: 376.
20. McConnell HM. *J. Chem. Phys.* 1958; **28**: 430.
21. Spiess HW. *Adv. Polym. Sci.* 1985; **66**: 23.
22. Brüschweiler R, Wright PE. *J. Am. Chem. Soc.* 1994; **116**: 8426.
23. Lipari G, Szabo A. *J. Am. Chem. Soc.* 1982; **104**: 4546.
24. Jelsch C, Teeter MM, Lamzin V, Pichon-Pesme V, Blessing RH, Lecomte C. *Proc. Natl. Acad. Sci. U.S.A.* 2000; **97**: 3171.
25. Cornilescu G, Bax A. *J. Am. Chem. Soc.* 2000; **122**: 10143.
26. Canet D. *Prog. Nucl. Magn. Reson. Spectrosc.* 1989; **21**: 237.
27. Haeberlen U. High resolution NMR in solids. selective averaging. In *Advances in Magnetic Resonance*, Suppl. 1, Waugh JS (ed). Academic Press: New York, 1976.
28. Hodgkinson P, Emsley L. *Prog. Nucl. Magn. Reson. Spectrosc.* 2000; **36**: 201.
29. Fliege J, Maier U. *IMA J. Numer. Anal.* 1999; **19**: 317.
30. Bystrov VF. *Prog. Nucl. Magn. Reson. Spectrosc.* 1976; **10**: 41.
31. Kroenke CD, Rance M, Palmer AG. *J. Am. Chem. Soc.* 1999; **121**: 10119.
32. Levitt MH. *J. Magn. Reson.* 1997; **126**: 164.
33. Rothwell WP, Waugh JS. *J. Chem. Phys.* 1981; **74**: 2721.
34. Loth K, Pelupessy P, Bodenhausen G. *J. Am. Chem. Soc.* 2005; **127**: 6062.
35. Sein J, Giraud N, Blackledge M, Emsley L. *J. Magn. Reson.* 2007; **186**: 26.
36. Herzfeld J, Berger AE. *J. Chem. Phys.* 1980; **73**: 6021.
37. Schmidt-Rohr K, Spiess HW. *Multidimensional Solid-State NMR and Polymers*. Academic Press: London, 1999.
38. Torchia DA, Szabo A. *J. Magn. Reson.* 1982; **49**: 107.
39. London RE, Avitabile J. *J. Am. Chem. Soc.* 1977; **99**: 7765.
40. Wittebort RJ, Szabo A. *J. Chem. Phys.* 1978; **69**: 1722.

41. Kroenke CD, Loria JP, Lee LK, Rance M, Palmer AG. *J. Am. Chem. Soc.* 1998; **120**: 7905.
42. Giraud N, Blackledge M, Goldman M, Böckmann A, Lesage A, Penin F, Emsley L. *J. Am. Chem. Soc.* 2005; **127**: 18190.
43. Varshalovich DA, Moskalev AN, Khersonskii VK. *Quantum Theory of Angular Momentum*. World Scientific: Singapore, 1988.
44. Redfield AG. *IBM J. Res. Dev.* 1957; **1**: 19.
45. Note that in practice a constant-time scheme which combines and can be advantageous. See Brutscher B. *Concepts Magn. Reson.* 2000; **12**: 207.
46. Clore GM, Szabo A, Bax A, Kay LE, Driscoll PC, Gronenborn AM. *J. Am. Chem. Soc.* 1990; **112**: 4989.
47. Bouvignies G, Bernado P, Meier S, Cho K, Grzesiek S, Brüschweiler R, Blackledge M. *Proc. Natl. Acad. Sci. U.S.A.* 2005; **102**: 13885.
48. Cole HBR, Torchia DA. *Chem. Phys.* 1991; **158**: 271.
49. North CL, Cross TA. *Biochemistry* 1995; **34**: 5883.
50. Mack JW, Usha MG, Long J, Griffin RG, Wittebort RJ. *Biopolymers* 2000; **53**: 9.
51. Chevelkov V, Zhuravleva AV, Xue Y, Reif B, Skrynnikov NR. *J. Am. Chem. Soc.* 2007; **129**: 12594.
52. Millet O, Loria JP, Kroenke CD, Pons M, Palmer AG. *J. Am. Chem. Soc.* 2000; **122**: 2867.
53. Palmer AG, Kroenke CD, Loria JP. *Methods Enzymol.* 2001; **339**: 204.
54. McDermott AE. *Curr. Opin. Struct. Biol.* 2004; **14**: 554.
55. Reif B, Xue Y, Agarwal V, Pavlova MS, Hologne M, Diehl A, Ryabov YE, Skrynnikov NR. *J. Am. Chem. Soc.* 2006; **128**: 12354.
56. Chen JH, Brooks CL, Wright PE. *J. Biomol. NMR* 2004; **29**: 243.
57. Lakomek NA, Farès C, Becker S, Carlomagno T, Meiler J, Griesinger C. *Angew. Chem. Int. Ed.* 2005; **44**: 7776.

DOI: 10.1002/mrc